Soft Matter

Chiral self-sorting of active semiflexible filaments with intrinsic curvature

Journal:	*Soft Matter*
Manuscript ID	SM-ART-06-2020-001163.R1
Article Type:	Paper
Date Submitted by the Author:	10-Feb-2021
Complete List of Authors:	Moore, Jeffrey; University of Colorado Boulder, Physics Glaser, Matthew; University of Colorado Boulder, Department of Physics Betterton, Meredith; University of Colorado Boulder, Physics

Journal Name

ARTICLE TYPE

Cite this: DOI: 00.0000/xxxxxxxxxx

Chiral self-sorting of active semiflexible filaments with intrinsic curvature†

Jeffrey M Moore,[a] Matthew A. Glaser,[a] and Meredith D. Betterton[ab]‡

Received Date
Accepted Date

DOI: 00.0000/xxxxxxxxxx

Many-body interactions in systems of active matter can cause particles to move collectively and self-organize into dynamic structures with long-range order. In cells, the self-assembly of cytoskeletal filaments is critical for cellular motility, structure, intracellular transport, and division. Semiflexible cytoskeletal filaments driven by polymerization or motor-protein interactions on a two-dimensional substrate, such as the cell cortex, can induce filament bending and curvature leading to interesting collective behavior. For example, the bacterial cell-division filament FtsZ is known to have intrinsic curvature that causes it to self-organize into rings and vortices, and recent experiments reconstituting the collective motion of microtubules driven by motor proteins on a surface have observed chiral symmetry breaking of the collective behavior due to motor-induced curvature of the filaments. Previous work on the self-organization of driven filament systems have not studied the effects of curvature and filament structure on collective behavior. In this work, we present Brownian dynamics simulation results of driven semiflexible filaments with intrinsic curvature and investigate how the interplay between filament rigidity and radius of curvature can tune the self-organization behavior in homochiral systems and heterochiral mixtures. We find a curvature-induced reorganization from polar flocks to self-sorted chiral clusters, which is modified by filament flexibility. This transition changes filament transport from ballistic to diffusive at long timescales.

1 Introduction

Active matter systems with particles that are driven can self-organize into structures that exhibit emergent dynamical order on length scales many times greater than the scale of a single particle. In cells, the dynamic self-assembly of cytoskeletal filaments driven by polymerization, motor proteins, and crosslinkers is necessary for the production of macromolecular assemblies, such as the mitotic spindle[1–4]. Most previous theoretical studies of cytoskeletal self-assembly have assumed rigid and straight filaments, but recent experiments have identified self-organization behavior due to filament curvature. Experiments reconstituted collective self-assembly by driving filaments on a surface with bound motor proteins[5–11]. Microtubules can undergo chiral symmetry breaking due to induced curvature mediated by motors, causing the filaments to self-organize into a dynamic lattice of vortices[9], or rotating polar streams[11]. In addition, *in vivo* observations of the bacterial cytoskeletal filament FtsZ found that intrinsic curvature led to the formation of dynamic bundles of curved rings and vortices[12,13]. These findings motivate further study of the collective behavior of driven filaments with curvature.

Previous theoretical studies of active systems with chirality have also taken their inspiration from biological systems. Swimming sperm cells[14,15], confined bacteria[16,17], and *E. coli* swimming near a solid interface[18,19] all exhibit chiral behavior. Brownian dynamics simulations have been used to predict the collective behavior of chiral microswimmers, and found phase separation of particles into spatially-segregated clusters[20–23], activity-induced chiral self-sorting of heterochiral mixtures[24,25], demixing of differently-shaped particles[26], and stable vortex arrays of circle swimmers[27,28]. There have, however, been few theoretical studies of active curved filaments. Previous work includes simulations of FtsZ filaments with varying particle density and noise strength[29], and passive filaments in the presence of a swirling flow[30]. FtsZ, microtubules, and f-actin each have different stiffness and intrinsic or induced curvature. Therefore, this work focuses on self-organization of driven curved filaments over a range

[a] *Department of Physics, University of Colorado, Boulder, CO, 80309, USA.*
[b] *Department of Molecular, Cellular, and Developmental Biology, University of Colorado, Boulder, CO 80309, USA. E-mail: mdb@colorado.edu*

† Electronic Supplementary Information (ESI†) available: [details of any supplementary information available should be included here]. See DOI: 00.0000/00000000.

‡ To whom correspondence should be addressed.

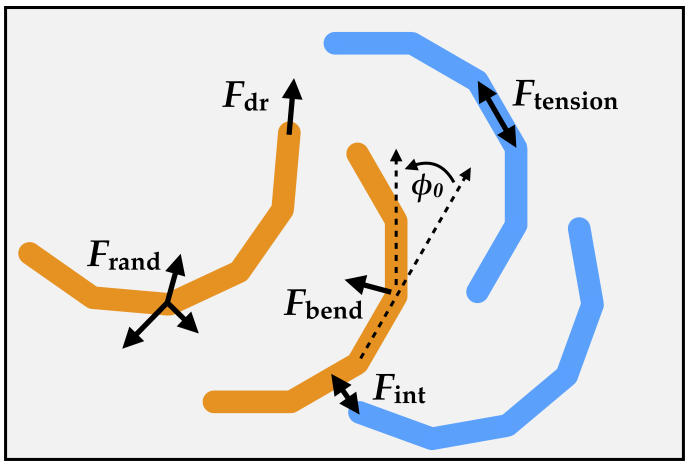

Fig. 1 Schematic of the model and forces acting on filaments. Filaments are discretized wormlike chains composed of multiple rigid segments. Filaments are subject to driving forces $\mathbf{F}_{dr}$, a bending force $\mathbf{F}_{bend}$, interaction forces $\mathbf{F}_{int}$, a tension force $\mathbf{F}_{tension}$, and random forces $\mathbf{F}_{rand}$. The polar driving forces are tangent to all filament segments and control system activity. The bending force maintains an intrinsic curvature with equilibrium angle ϕ_0 between filament segments. The interaction forces model steric repulsion between filaments. The tension force maintains the rigid segment length constraints. The random thermal forces give rise to Brownian motion of the filament.

of bending rigidity and radius of curvature.

In this work, we present results of Brownian dynamics simulations of active semiflexible filaments. We study both homochiral and heterochiral systems and vary filament bending rigidity, radius of curvature, packing fraction, and aspect ratio. The collective behavior depends strongly on filament flexibility and curvature: as the curvature increases, there is a dramatic reorganization of the phase behavior from polar flocking to self-sorted chiral clusters. However, the transition is weakened or lost if the filaments are too flexible.

2 Model and simulation

Our Brownian dynamics simulations are two-dimensional with periodic boundary conditions of N filaments with intrinsic curvature. Following previous work[31,32], the filaments in our simulations are modeled as discretized wormlike chains[33] composed of n sites and $n-1$ rigid segments of fixed length a. We adopt the algorithm of Montesi et. al[34] for constrained Brownian dynamics of bead-rod wormlike chains. The n site positions are updated according to inertialess Langevin equation

$$\dot{\mathbf{r}}_i = \zeta_i^{-1}\mathbf{F}_i, \tag{1}$$

where ζ is an anisotropic friction tensor with parallel and perpendicular components $\zeta_\perp = 2\zeta_\parallel$, and site forces

$$\mathbf{F}_i = \mathbf{F}_i^{dr} + \mathbf{F}_i^{bend} + \mathbf{F}_i^{int} + \mathbf{F}_i^{tension} + \mathbf{F}_i^{rand}, \tag{2}$$

include driving forces $\mathbf{F}_{dr}$, bending forces $\mathbf{F}_{bend}$, filament-filament interaction forces $\mathbf{F}_{int}$, tension forces $\mathbf{F}_{tension}$, and random thermal forces $\mathbf{F}_{rand}$ (Fig. 1).

Filament activity is induced by a polar driving force per unit length f_{dr} acting tangent to each of the filament segments, $\mathbf{F}_i^{dr} = af_{dr}\mathbf{u}_i$. The activity of the system is measured by the Péclet number, the ratio of active to diffusive transport. For straight and rigid filaments, the characteristic timescale for active transport is the time required for the filament moving at velocity v to traverse a distance equal its own length L, $\tau_A = L/v = \zeta_\parallel L/F_{dr}$. The time for a filament to diffuse its own length is $\tau_D = L^2/D_\parallel = \zeta_\parallel L^2/k_BT$; thus the Péclet number is $\mathrm{Pe} = \tau_D/\tau_A = f_{dr}L^2/k_BT$. In the case of curved filaments, the mean-squared displacement and therefore the effective active transport can differ, as discussed later. We continue to use this definition of the Péclet number for consistency.

Filament bending forces are derived from the bending potential of a continuous wormlike chain $\frac{\kappa}{2}\int_0^L (R^{-1}(s) - R_0^{-1})^2\,ds$, where $R(s)$ is the local radius of curvature with respect to the contour length s for a length L filament, and R_0 is a radius of curvature that corresponds to an intrinsic curvature per unit length $R_0^{-1} = d\phi/ds$. The persistence length of the filament is related to the bending rigidity as $L_p k_BT = \kappa$. In a discrete wormlike chain model, the bending potential is

$$U_{bend} = -\frac{\kappa}{a}\sum_{i=2}^{n-1}\cos(\theta_{i,i-1} - \phi_0), \tag{3}$$

where $\theta_{i,j} = \arccos(\mathbf{u}_i \cdot \mathbf{u}_j)$ is the angle between segments i and j, and $\phi_0 = ad\phi/ds$ corresponds to the expected angle between two segments of length a and intrinsic curvature per unit length $d\phi/ds$.

Steric repulsion between filaments $\mathbf{F}_{int}$ is modeled by a Weeks-Chandler-Andersen (WCA) potential,

$$U_{WCA} = \left(4\varepsilon\left(\left(\frac{\sigma}{r_{ij}}\right)^{12} - \left(\frac{\sigma}{r_{ij}}\right)^{6}\right) + \varepsilon\right)\left(1 - \Theta(2^{1/6}\sigma)\right), \tag{4}$$

where r_{ij} is the minimum distance between two filaments, σ is the filament diameter, $\varepsilon = k_BT$ is the energy scale and Θ is the Heaviside step function.

To model the wormlike chain as an inextensibile filament with rigid bonds, the model is subject to constraints for the segment length $|\mathbf{r}_i - \mathbf{r}_{i-1}| = a$. A tension force is necessary to prevent external forces from violating the constraints, restricting the dynamics of the N filament sites to a constrained subspace[35].

The random forces $\mathbf{F}_{rand}$ applied to each site are due to thermal contact with a heat bath at temperature T. The components of the random forces $F_{rand}^{(k)}$ are delta-correlated random variables with mean $\langle F_{rand}^{(k)}(t)\rangle = 0$ and variance $\langle F_{rand}^{(k)}(t)F_{rand}^{(k)}(t')\rangle = 2k_BT\zeta\delta(t - t')$ as dictated by the fluctuation-dissipation theorem. The random forces are then geometrically projected to prevent violation of the segment length constraints (see ESI†).

The characteristic length and energy scales in our simulation are the filament diameter σ and k_BT. We use dimensionless units: the dimensionless lengths for our system are the aspect ratio $\tilde{L} = L/\sigma$, the bending rigidity $\tilde{\kappa} = \kappa/Lk_BT = L_p/L$, and radius of curvature $\tilde{R} = R/L$. The packing fraction $\phi = A_{fil}/A_{sys}$, where A_{fil} is the combined area of all N filaments and A_{sys} is the periodic area of the system. In our simulations, we vary the bending rigidity from $\tilde{\kappa} = 10$–1000 and the radius of curvature from $\tilde{R} = 0.25$–2, as well as straight filaments with $\tilde{R} = \infty$. We also examine two fil-

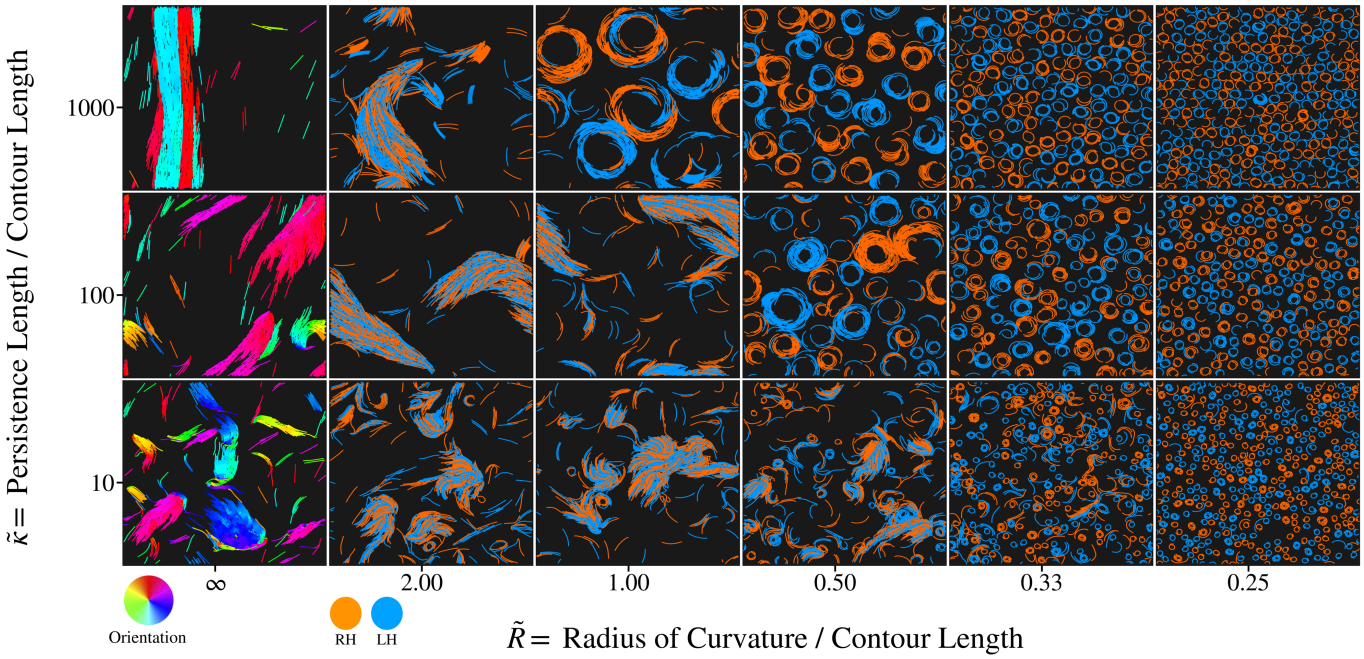

Fig. 2 Simulation images depicting the collective behavior for heterochiral filaments of $\tilde{L} = 20$ and $\phi = 0.25$ for different values of filament stiffness $\tilde{\kappa}$ and radius of curvature $\tilde{R}$. The filaments are colored according to their orientation in the case of $\tilde{R} = \infty$ and according to their handedness otherwise, with orange and blue labeling curved filaments with right- and left-handed chirality respectively.

ament densities $\phi = 0.25$ and 0.5, two aspect ratios $\tilde{L} = 10$ and 20, and both homochiral systems and 1:1 heterochiral mixtures. Simulations were run for $10^3 - 10^4 \tau_A$. Further discussion of computational details is available in the ESI†.

3 Results

3.1 Formation of chiral clusters

Driven curved filaments undergo a dramatic reorganization from polar flocks to chiral clusters, induced by filament curvature and tuned by filament flexibility (see Fig. 2). Driven achiral filaments ($\tilde{R} = \infty$) form polar flocks or a swirling phase depending on filament rigidity and density. Chiral filaments with large radius of curvature ($\tilde{R} = 2$) form flocks of bent heterochiral filaments, leading to curved flock trajectories and buckling at higher densities. At low radius of curvature ($\tilde{R} < 1$), there is a transition from polar heterochiral flocks to self-sorted homochiral clusters. Filament flexibility delays the onset of chiral clustering as the radius of curvature decreases.

In the absence of curvature, achiral driven filaments aggregate into well-known polar flocks[32,36–41], with structural order that is dependent on filament bending rigidity, as shown in previous work[32,42]. Driven flexible filaments can form an active disordered phase of swirling defects[17,43,44]. Chiral filaments with large radius of curvature ($\tilde{R} = 2$) can form heterochiral flocks composed of filaments with mixed handedness that are stable due to the deformability of the filaments.

With decreasing radius of curvature, the system undergoes a curvature-induced transition from polar flocks to chiral clusters. The lower radius of curvature increases the bending energy required to deform filaments into stable heterochiral flocks, so activity drives filaments into spatially-segregated domains of high filament density (see Fig. 2, $\tilde{\kappa} = 100$, $\tilde{R} = 0.5$). Filaments of opposite handedness are rarely colocalized due to frequent collisions and fast decorrelation of their trajectories. Chiral self-sorting has been reported in previous studies of active chiral systems with spinning rotors[24,45] and Vicsek-type models of chiral microswimmers[25], where self-sorting occurs at a macroscopic scale. In our model, steric repulsion between filaments and curved filament shape cause filaments to self-organize into a disordered lattice of self-sorted chiral vortices. Filament flexibility delays the onset of the transition to chiral clusters because it allows greater deformation away from the preferred curvature. Filament bending rigidity therefore tunes the long-range structural order of driven achiral filaments and the self-sorting behavior of active curved filaments.

In the flocking phase, rigid filaments form giant flocking domains that dominate the structure of the system, leading to strong nematic alignment. Flexible filaments form coexisting flocks with a distribution of sizes. The flocks are dynamic structures, with filaments continuously joining and leaving the flocks, though giant flocks are more stable and long-lived due to a large number of kinetically-trapped filaments at the flock interior[40,46–48]. When the radius of curvature is large, curved filaments of mixed handedness can form heterochiral flocks due to the finite rigidity of the filaments. Comoving filaments with opposite chirality deform into internally jammed polar flocks. Filaments in the flock interior have low curvature while deformed, and therefore stay aligned to maintain stable giant flocks or nematic bands (see Fig. 2, $\tilde{\kappa} = 100$, $\tilde{R} = 2$). However, more rigid filaments tend to form packed layers (see Fig. 2, $\tilde{\kappa} = 1000$, $\tilde{R} = 2$) reminiscent of smectic liquid crystals[48–50]. This packing reduces interweaving between filament layers, and thereby decreases the stability of large flocks, even in entirely homochiral systems (see ESI†). Therefore, filament cur-

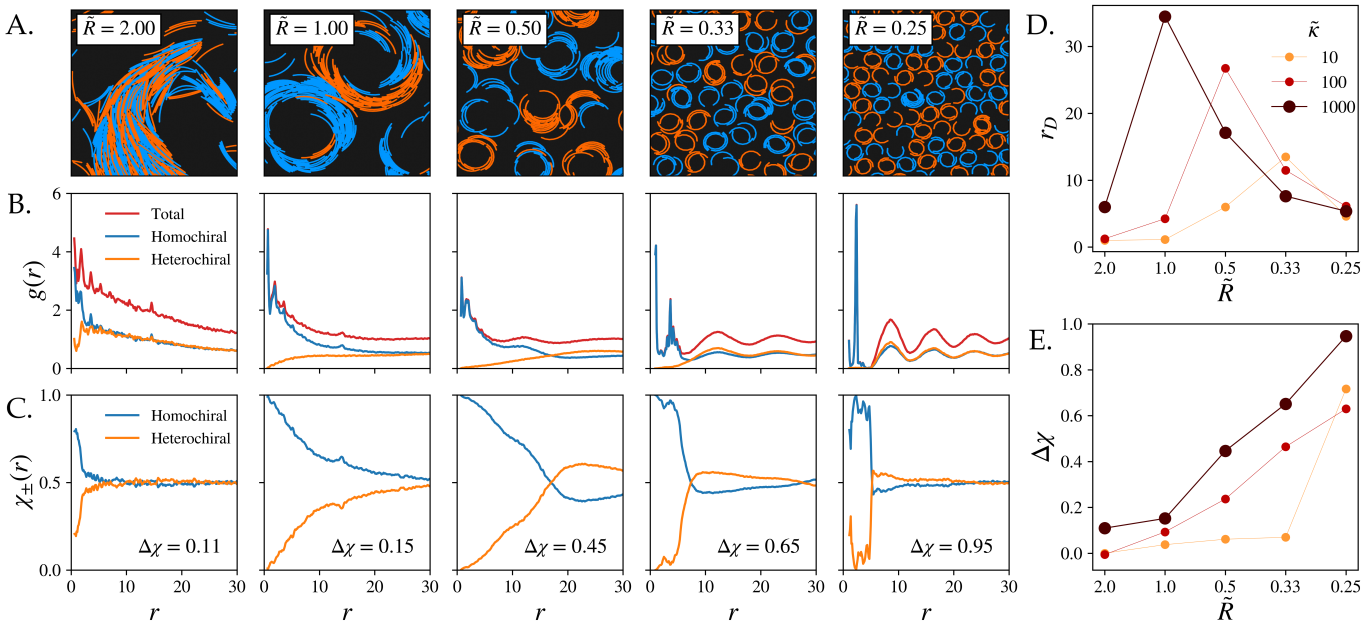

Fig. 3 A) Simulation images of collective behavior for different filament radius of curvature, with $\tilde{L} = 20$, $\phi = 0.25$, and $\tilde{\kappa} = 1000$. B) Radial distribution function $g(r)$ for filaments corresponding to the simulation images in A. The distribution function is plotted as the total distribution between all filaments (red), between homochiral filaments (blue), and between heterochiral filaments (orange). r is measured in units of the filament diameter, σ. C) Chiral order parameter $\chi_{\pm}(r)$ for homochiral (blue) and heterochiral (orange) filaments. The corresponding chiral sorting parameter $\Delta\chi$ is included in the bottom right of the figures. D) Domain radius r_D versus $\tilde{R}$ plotted for $\tilde{L} = 20$, $\phi = 0.25$. E) Chiral sorting parameter $\Delta\chi$ versus $\tilde{R}$ for $\tilde{L} = 20$, $\phi = 0.25$.

vature causes rigid filaments to have lower long-range structural order than flexible filaments, a reversal of what has been previously reported for achiral semiflexible filament behavior[32,42].

3.2 Chiral self-sorting

To better understand how filament curvature and bending rigidity affect the self-organization of chiral clusters, we quantified the structure and sorting in our systems by measuring the radial distribution function. The radial distribution function $g(r)$ is defined for a 2D system with particle density ρ such that $\langle 2\pi r dr\rangle \rho g(r)$ is the number of particles in a circular annulus of width dr at a distance r from a reference particle, averaged over the particle ensemble:

$$g(r) = \frac{2\pi}{N\rho}\sum_{i=1}^{N}\int_{r}^{r+dr'}\sum_{j\neq i}\delta\left(\mathbf{r}' - (\mathbf{r_j} - \mathbf{r_i})\right)r'\,dr', \tag{5}$$

where $\delta(x)$ is the Dirac delta function. The radial distribution functions for homochiral and heterochiral particles, $g_+(r)$ and $g_-(r)$, were also calculated by adding the factor $\delta_{\pm\chi_i\chi_j}$ in the second sum in Eqn. 5, where δ_{ij} is the Kronecker delta function and $\chi = \pm 1$ for right- and left-handed chiral particles, respectively.

Activity drives an increase in local particle density due to flocking and clustering behavior, indicated by a peak in $g(r)$ for $r \approx \sigma$ (Fig. 3B). In the chiral cluster phase, the peak is largely composed of homochiral filaments due to chiral sorting. The local density of heterochiral particles is suppressed below a length scale that specifies the sorted domain size, which depends on the radius of curvature and flexibility.

To quantify chiral sorting, we define a chiral structural order parameter $\chi_{\pm}(r) = g_{\pm}(r)/g(r)$ that measures the average homo/heterochiral sorting as function of distance r from a reference particle. For a sorted system, $\chi_+(r)$ is strictly greater than $\chi_-(r)$ for $r < r_D$, where r_D is the sorted domain radius, defined to be the first point at which $\chi_+(r) = \chi_-(r)$. The extent of chiral sorting within the domain is given by the chiral sorting order parameter

$$\Delta\chi = \frac{\int_0^{r_D}\left(g_+(r) - g_-(r)\right)r\,dr}{\int_0^{r_D} g(r)\,r\,dr}, \tag{6}$$

which is the fraction of homochiral particles within the sorted domain, and varies from 0–1 due to the definition of r_D. Thus r_D measures the typical size of sorted domains and $\Delta\chi$ the degree of sorting within a domain.

The domain radius r_D is largest near the transition between heterochiral flocking behavior and chiral self-sorting due to the large $\tilde{R}$ of filaments within the sorted cluster. r_D typically decreases as $\tilde{R}$ decreases, as one would expect due to filament trajectories following smaller circular paths (Fig. 3D). Interestingly, the degree of chiral sorting increases with decreasing $\tilde{R}$ (Fig. 3E). This is due to smaller domains having more efficient packing within the system, and therefore fewer collisions between clusters result in fewer opportunities for filaments to intermix between sorted domains. Filament flexibility weakens chiral sorting due to filament deformation, consistent with our observations that flexibility weakens structural order in systems of driven filaments[32]. Flexible filaments collide and form heterochiral flocks, which perturb chiral clusters with collisions, increasing mixing. In addition, the transition between phases of heterochiral flocking and chiral clusters is sharper for rigid filaments, whereas flexible filaments exhibit coexistence between the two states, and only be-

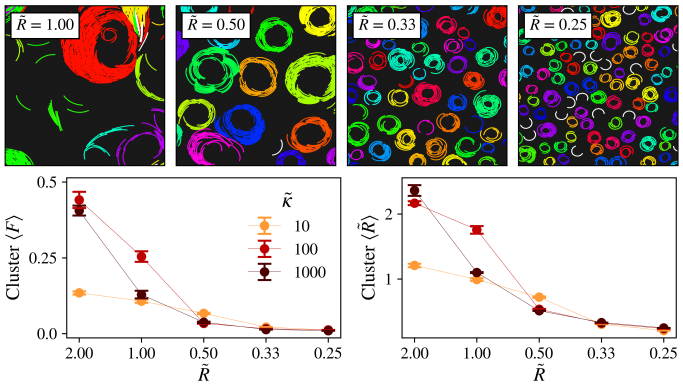

Fig. 4 Top: simulation images of filament clusters for different filament radius of curvature. Clusters are labeled by color. Unclustered filaments are shown in white. Bottom left: time-averaged cluster filament fraction $\langle F \rangle$, which is the average number of filaments per cluster normalized by the number of filaments in the simulation, and plotted as a function of filament radius of curvature. Bottom right: mean cluster radius of curvature $\langle \tilde{R} \rangle$ as a function of filament radius of curvature $\tilde{R}$.

come sorted at the smallest radius of curvature examined here.

3.3 Cluster dynamics and filament transport

To better understand the dynamical behavior of filament clusters, we developed a method to identify clustered filaments. Filaments were clustered by their centers of curvature $\mathbf{r}_c(t)$, determined from the filaments' instantaneous radius of curvature $R(t)$ averaged over the contour length of the filament (Fig. 4). Cluster positions are the average of their constituent filament centers of curvature, $\mathbf{r}_C(t) = \frac{1}{n}\sum_i^n \mathbf{r}_c^{(i)}(t)$, and the cluster radius is defined to be the average of the constituent filament radius of curvature $R_c(t) = \frac{1}{n}\sum_i^n R_i(t)$. Unclustered filaments can join an existing cluster when $|\mathbf{r}_c^{(i)}(t) - \mathbf{r}_C(t)| \leq R_c(t)$ for a time interval of τ_A (see ESI†).

The mean cluster radius $\langle \tilde{R} \rangle$ decreases with radius of curvature as expected. The mean number of filaments in an average cluster also decreases with cluster size, since steric effects put an upper limit on the filament density within small clustered domains. Filament number is reported as a fraction of filaments in the system per cluster on average $\langle F \rangle$, with brackets $\langle ... \rangle$ denoting a time and ensemble average. Only clusters with lifetimes longer than τ_A are considered in our analysis to ensure a low false discovery rate.

The circular motion of clustered filaments drastically alters the transport of filaments compared to the ballistic motion of flocks, and we find that clusters of different sizes have different transport behavior. The transport of filaments is measured by the mean-squared displacement (MSD) $\langle (\mathbf{r}(t) - \mathbf{r}(0))^2 \rangle$. At short times, the MSD for clustered filaments is subdiffusive, and approaches the diffusive regime at late times (Fig. 5). We extracted a diffusion constant from the MSD using the relationship $\langle (\mathbf{r}(t) - \mathbf{r}(0))^2 \rangle \propto Dt^\alpha$ with $\alpha = 1$ indicating diffusive transport, and superdiffusive and subdiffusive transport being indicated for $\alpha > 1$ and $\alpha < 1$ respectively. The activity of curved filaments leads to circular trajectories and subdiffusive transport at short timescales, and diffusive dynamics at long timescales as filaments are able to escape the confinement of their clusters.

The MSD of individual active filaments is superdiffusive for achiral filaments, and diffusive at long timescales for curved filaments (see ESI†). This result is analogous to previous studies of diffusive behavior for circle swimmers[51,52], where particle torque plays a similar role as filament curvature. In collective systems, curved and achiral filaments that form flocks ($\tilde{R} > 1$) have superdiffusive transport due to the ballistic motion of flocks. Curved filaments that form clusters are subdiffusive at short times, with a rotational periodicity of the MSD that dampens over time, while their long-time behavior is diffusive. When the radius of curvature is small ($\tilde{R} \leq 0.5$), the filaments become entangled with a small number of particles[47] and are kinetically trapped for long times, causing infrequent intermixing of filaments between clusters and increasing cluster stability and lifetime. Comparing the clustering structure and dynamics for homochiral and heterochiral systems, we did not find significant deviations in clustering behavior for the range of parameters examined here (see ESI†).

Even at late times, the diffusivity of active filaments is lower than that of passive filaments, indicating that activity leads to an effective freezing of the system dynamics[53]. Flexible filaments with $\tilde{R} = 0.25$ remain subdiffusive even at long times, likely due to the filaments self-interacting and coiling into spirals (see ESI†), which alters the filament MSD compared to clusters of more rigid filaments. The formation of spirals by driven filaments due to self-interactions have been observed in experiments, even for stiff microtubules[7,8].

4 Conclusions

The patterns of clusters in our simulations are similar to those of previous experiments that observed the formation of a lattice of vortices[7,9]. In our simulations, the size and stability of the vortices vary depending on filament curvature and bending rigidity, and are chirally self-sorted for systems of heterochiral filaments. Unlike previous work with active spinning rotors[24,45] or active Brownian particles with Vicsek-type alignment interactions[20,25], we do not see evidence of macroscopic sorting of clusters into large homochiral domains. Our analysis of the arrangement of the clusters found that the arrangement did not vary significantly from random (see ESI†), implying that chiral self-sorting of active curved filaments only occurs at length scales on the order of the filament radius of curvature. This is because the cluster shapes examined here are approximately convex and experience low friction between neighboring domains of opposite chirality. Together with the slow dynamics of filaments with small radius of curvature, macroscopic sorting is unfavorable in these systems.

The results of our Brownian dynamics simulations show that the self-organization of driven semiflexible filaments can undergo a transition between polar flocks and chiral clusters that is tuned by filament curvature and bending rigidity. Our model predicts the collective behavior of future filament gliding experiments for filaments of different persistence lengths that may have intrinsic or induced curvature, and may also have applications for the study of transport behavior for self-assembled curved biopolymers such as FtsZ.

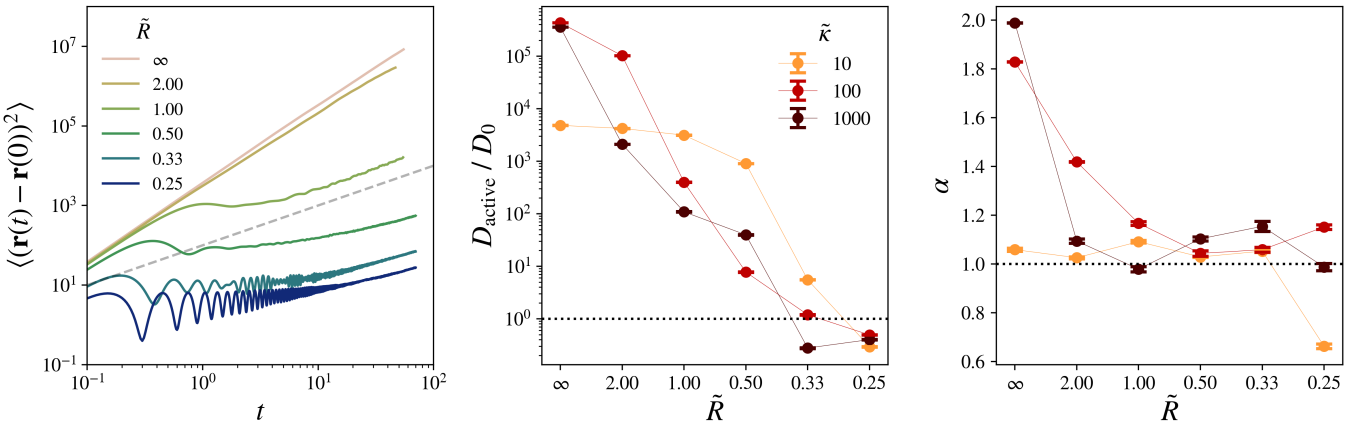

Fig. 5 Left: mean-squared displacement (MSD) for active filaments of length $\tilde{L} = 10$, filament density $\phi = 0.25$, and stiffness $\tilde{\kappa} = 1000$ for different values of radius of curvature. The time axis t is measured in units of τ_A. The average MSD is subdiffusive at short timescales and becomes diffusive at longer timescales. Center: Effective diffusion constants D_{active} extracted from the final $20\tau_A$ of accessible simulation time assuming linear time scaling. The effective diffusion constant is normalized by diffusion constant of inactive filaments D_0 for otherwise identical simulation parameters (see ESI†). Right: time scaling exponent α extracted from the late-time MSD used to calculated D_{active}. The transport of filaments that form smaller flocks and clusters approach diffusive transport at late times, while the ballistic motion of giant flocks produces superdiffusive behavior ($\alpha > 1$).

Conflicts of interest

There are no conflicts to declare.

Acknowledgements

We would like to acknowledge funding for this work from the Soft Materials Research Center under NSF MRSEC Grant No. DMR-1420736, and the National Science Foundation under NSF GRFP Award No. DGE-1144083 and NSF Grant No. DMR-1725065. This work utilized the RMACC Summit supercomputer, which is supported by the National Science Foundation (awards ACI-1532235 and ACI-1532236), the University of Colorado Boulder, and Colorado State University. The Summit supercomputer is a joint effort of the University of Colorado Boulder and Colorado State University.

Notes and references

1 A. A. Hyman and E. Karsenti, *Cell*, 1996, **84**, 401–410.
2 F. J. Nedelec, T. Surrey, A. C. Maggs and S. Leibler, *Nature*, 1997, **389**, 305–308.
3 T. Surrey, F. Nédélec, S. Leibler and E. Karsenti, *Science*, 2001, **292**, 1167–1171.
4 D. Needleman and Z. Dogic, *Nature Reviews Materials*, 2017, **2**, 17048.
5 T. Butt, T. Mufti, A. Humayun, P. B. Rosenthal, S. Khan, S. Khan and J. E. Molloy, *Journal of Biological Chemistry*, 2010, **285**, 4964–4974.
6 V. Schaller, C. Weber, C. Semmrich, E. Frey and A. R. Bausch, *Nature*, 2010, **467**, 73–77.
7 V. Schaller, C. A. Weber, B. Hammerich, E. Frey and A. R. Bausch, *Proceedings of the National Academy of Sciences*, 2011, **108**, 19183–19188.
8 L. Liu, E. Tüzel and J. L. Ross, *Journal of Physics: Condensed Matter*, 2011, **23**, 374104.
9 Y. Sumino, K. H. Nagai, Y. Shitaka, D. Tanaka, K. Yoshikawa, H. Chaté and K. Oiwa, *Nature*, 2012, **483**, 448–452.
10 L. Huber, R. Suzuki, T. Krüger, E. Frey and A. R. Bausch, *Science*, 2018, **361**, 255–258.
11 K. Kim, N. Yoshinaga, S. Bhattacharyya, H. Nakazawa, M. Umetsu and W. Teizer, *Soft Matter*, 2018, **14**, 3221–3231.
12 E. L. Meier and E. D. Goley, *Current Opinion in Cell Biology*, 2014, **26**, 19–27.
13 M. Loose and T. J. Mitchison, *Nature Cell Biology*, 2014, **16**, 38–46.
14 I. H. Riedel, K. Kruse and J. Howard, *Science*, 2005, **309**, 300–303.
15 B. M. Friedrich and F. Jülicher, *Proceedings of the National Academy of Sciences*, 2007, **104**, 13256–13261.
16 H. H. Wensink, J. Dunkel, S. Heidenreich, K. Drescher, R. E. Goldstein, H. Löwen and J. M. Yeomans, *Proceedings of the National Academy of Sciences*, 2012, **109**, 14308–14313.
17 H. Löwen, *The European Physical Journal Special Topics*, 2016, **225**, 2319–2331.
18 W. R. DiLuzio, L. Turner, M. Mayer, P. Garstecki, D. B. Weibel, H. C. Berg and G. M. Whitesides, *Nature*, 2005, **435**, 1271–1274.
19 E. Lauga, W. R. DiLuzio, G. M. Whitesides and H. A. Stone, *Biophysical Journal*, 2006, **90**, 400–412.
20 B. Liebchen and D. Levis, *Physical Review Letters*, 2017, **119**, 058002.
21 G.-J. Liao and S. H. L. Klapp, *Soft Matter*, 2018, **14**, 7873–7882.
22 D. Levis and B. Liebchen, *Journal of Physics: Condensed Matter*, 2018, **30**, 084001.
23 D. Levis and B. Liebchen, *Physical Review E*, 2019, **100**, 012406.
24 N. H. P. Nguyen, D. Klotsa, M. Engel and S. C. Glotzer, *Physical Review Letters*, 2014, **112**, 075701.

25 D. Levis, I. Pagonabarraga and B. Liebchen, *Physical Review Research*, 2019, **1**, 023026.

26 H. H. Wensink, V. Kantsler, R. E. Goldstein and J. Dunkel, *Physical Review E*, 2014, **89**, 010302.

27 A. Kaiser and H. Löwen, *Physical Review E*, 2013, **87**, 032712.

28 Y. Yang, F. Qiu and G. Gompper, *Physical Review E*, 2014, **89**, 012720.

29 J. Denk, L. Huber, E. Reithmann and E. Frey, *Physical Review Letters*, 2016, **116**, 178301.

30 N. Küchler, H. Löwen and A. M. Menzel, *Physical Review E*, 2016, **93**, 022610.

31 J. M. Moore, *C-GLASS: A Coarse-Grained Living Active Systems Simulator*, Zenodo, 2020, 10.5281/zenodo.3841613.

32 J. M. Moore, T. N. Thompson, M. A. Glaser and M. D. Betterton, *Soft Matter*, 2020, **16**, 9436–9442.

33 O. Kratky and G. Porod, *Recueil des Travaux Chimiques des Pays-Bas*, 1949, **68**, 1106–1122.

34 A. Montesi, D. C. Morse and M. Pasquali, *The Journal of Chemical Physics*, 2005, **122**, 084903.

35 D. C. Morse, in *Theory of Constrained Brownian Motion*, John Wiley & Sons, Ltd, 2003, ch. 2, pp. 65–189.

36 T. Vicsek, A. Czirók, E. Ben-Jacob, I. Cohen and O. Shochet, *Physical Review Letters*, 1995, **75**, 1226–1229.

37 J. Toner and Y. Tu, *Physical Review Letters*, 1995, **75**, 4326–4329.

38 G. Grégoire and H. Chaté, *Physical Review Letters*, 2004, **92**, 025702.

39 F. Ginelli, F. Peruani, M. Bär and H. Chaté, *Physical Review Letters*, 2010, **104**, 184502.

40 H.-S. Kuan, R. Blackwell, L. E. Hough, M. A. Glaser and M. D. Betterton, *Phys. Rev. E*, 2015, **92**, 060501–060506.

41 F. Ginelli, *The European Physical Journal Special Topics*, 2016, **225**, 2099–2117.

42 Ö. Duman, R. E. Isele-Holder, J. Elgeti and G. Gompper, *Soft Matter*, 2018, **14**, 4483–4494.

43 T. Sanchez, D. T. N. Chen, S. J. DeCamp, M. Heymann and Z. Dogic, *Nature*, 2012, **491**, 431–434.

44 A. Opathalage, M. M. Norton, M. P. N. Juniper, B. Langeslay, S. A. Aghvami, S. Fraden and Z. Dogic, *Proceedings of the National Academy of Sciences*, 2019, **116**, 4788–4797.

45 C. Scholz, M. Engel and T. Pöschel, *Nature Communications*, 2018, **9**, 1–8.

46 A. J. Liu and S. R. Nagel, *Nature*, 1998, **396**, 21–22.

47 N. Gravish, S. V. Franklin, D. L. Hu and D. I. Goldman, *Physical Review Letters*, 2012, **108**, 208001.

48 C. Avendaño and F. A. Escobedo, *Current Opinion in Colloid & Interface Science*, 2017, **30**, 62–69.

49 H. F. Leube and H. Finkelmann, *Die Makromolekulare Chemie*, 1990, **191**, 2707–2715.

50 H. R. Brand, P. E. Cladis and H. Pleiner, *Macromolecules*, 1992, **25**, 7223–7226.

51 S. van Teeffelen and H. Löwen, *Phys. Rev. E*, 2008, **78**, 020101–020104.

52 C. Weber, P. K. Radtke, L. Schimansky-Geier and P. Hänggi, *Phys. Rev. E*, 2011, **84**, 011132–011139.

53 C. Reichhardt and C. J. O. Reichhardt, *Proceedings of the National Academy of Sciences*, 2011, **108**, 19099–19100.